

Distribution and compositional variations of plasma ions in Mercury's space environment: The first three Mercury years of MESSENGER observations

Jim M. Raines,¹ Daniel J. Gershman,¹ Thomas H. Zurbuchen,¹ Menelaos Sarantos,^{2,3} James A. Slavin,¹ Jason A. Gilbert,¹ Haje Korth,⁴ Brian J. Anderson,⁴ George Gloeckler,¹ Stamatis M. Krimigis,^{4,5} Daniel N. Baker,⁶ Ralph L. McNutt Jr.,⁴ and Sean C. Solomon^{7,8}

Received 27 June 2012; revised 18 October 2012; accepted 13 November 2012; published 29 April 2013.

[1] We have analyzed measurements of planetary ions near Mercury made by the Mercury Surface, Space ENvironment, GEochemistry, and Ranging (MESSENGER) Fast Imaging Plasma Spectrometer (FIPS) over the first three Mercury years of orbital observations (25 March 2011 through 31 December 2011). We determined the composition and spatial distributions of the most abundant species in the regions sampled by the MESSENGER spacecraft during that period. In particular, we here focus on altitude dependence and relative abundances of species in a variety of spatial domains. We used observed density as a proxy for ambient plasma density, because of limitations to the FIPS field of view. We find that the average observed density is $3.9 \times 10^{-2} \text{ cm}^{-3}$ for He^{2+} , $3.4 \times 10^{-4} \text{ cm}^{-3}$ for He^{+} , $8.0 \times 10^{-4} \text{ cm}^{-3}$ for O^{+} -group ions, and $5.1 \times 10^{-3} \text{ cm}^{-3}$ for Na^{+} -group ions. Na^{+} -group ions are particularly enhanced over other planetary ions (He^{+} and O^{+} group) in the northern magnetospheric cusp (by a factor of ~ 2.0) and in the premidnight sector on the nightside (by a factor of ~ 1.6). Within 30° of the equator, the average densities of all planetary ions are depressed at the subsolar point relative to the dawn and dusk terminators. The effect is largest for Na^{+} -group ions, which are 49% lower in density at the subsolar point than at the terminators. This depression could be an effect of the FIPS energy threshold. The three planetary ion species considered show distinct dependences on altitude and local time. The Na^{+} group has the smallest e -folding height at all dayside local times, whereas He^{+} has the largest. At the subsolar point, the e -folding height for Na^{+} -group ions is 590 km, and that for the O^{+} group and He^{+} is 1100 km. On the nightside and within 750 km of the geographic equator, Na^{+} -group ions are enhanced in the premidnight sector. This enhancement is consistent with nonadiabatic motion and may be observational evidence that nonadiabatic effects are important in Mercury's magnetosphere.

Citation: Raines, J. M., et al. (2012), Distribution and compositional variations of plasma ions in Mercury's space environment: The first three Mercury years of MESSENGER observations, *J. Geophys. Res. Space Physics*, 118, 1604–1619, doi:10.1029/2012JA018073.

1. Introduction

[2] The plasma environment at Mercury is determined by a complex interaction of plasma and neutral atom populations and competing processes involving Mercury's surface,

Mercury's atmosphere, solar photons, and the solar wind. Mercury's thin, collisionless atmosphere—a surface-bounded exosphere—is produced by a variety of processes that act on the surface of the planet. It is composed mainly of neutral H, He, Na, Mg, K, Ca, Al, and Fe atoms, although other constituents are expected [Broadfoot *et al.*, 1974;

This article was published online on 29 Apr 2013. An error was subsequently identified. This notice is included in the online and print versions to indicate that both have been corrected on 30 May 2013.

¹Department of Atmospheric, Oceanic and Space Sciences, University of Michigan, Ann Arbor, Michigan, USA.

²Heliophysics Science Division, NASA Goddard Space Flight Center, Greenbelt, Maryland, USA.

Corresponding author: J. M. Raines, Department of Atmospheric, Oceanic and Space Sciences, University of Michigan, Ann Arbor, MI 48109, USA. (jraines@umich.edu)

©2012. American Geophysical Union. All Rights Reserved.
2169-9380/13/2012JA018073

³Goddard Planetary Heliophysics Institute, University of Maryland, Baltimore County, Baltimore, Maryland, USA.

⁴The Johns Hopkins University Applied Physics Laboratory, Laurel, Maryland, USA.

⁵Office of Space Research and Technology, Academy of Athens, Athens, Greece.

⁶Laboratory for Atmospheric and Space Physics, University of Colorado, Boulder, Colorado, USA.

⁷Department of Terrestrial Magnetism, Carnegie Institution of Washington, Washington, D. C., USA.

⁸Lamont-Doherty Earth Observatory, Columbia University, Palisades, New York, USA.

Domingue et al., 2007; *Killen et al.*, 2007; *McClintock et al.*, 2009; *Bida et al.*, 2000]. These atoms may be on ballistic trajectories, in orbit around the planet, or on escape trajectories that are controlled by Mercury's gravity, their initial launch energy, and solar radiation pressure. Although the fraction of atoms escaping depends substantially on season, there is a sufficient population to form a persistent, although rarified, cloud around the planet [*Potter et al.*, 2007; *Leblanc and Johnson*, 2010; *Schmidt et al.*, 2012]. On the nightside, radiation pressure stretches this cloud into a comet-like neutral Na tail that extends more than 1000 Mercury radii (R_M) in the antisunward direction [*Potter et al.*, 2002; *Baumgardner et al.*, 2008; *Baumgardner and Mendillo*, 2009]. Ground-based telescopic studies [reviewed by *Killen et al.*, 2007] have shown large variations in inferred neutral column densities, their distribution through Mercury's atmosphere and space environment, and the relative abundances among the various species, both seasonally and on timescales of hours [*Potter and Morgan*, 1990, 1997; *Killen et al.*, 1990, 1999, 2001; *Killen*, 2005; *Sprague et al.*, 1997, 1998; *Potter et al.*, 1999; *Schmidt et al.*, 2012].

[3] The seasonal variability of the exosphere is related to changes in the solar photon intensity, the Doppler shift in the incident solar radiation, and the solar wind environment and micrometeoroid influx during Mercury's highly eccentric orbit, but it may also be related to a limited surface reservoir of volatiles [e.g., *Leblanc and Johnson*, 2003; *Killen et al.*, 2004; *Leblanc and Johnson*, 2010]. The observed variability of Na on the timescale of hours has been hypothesized to relate to variations in Mercury's local space environment, including variations in solar wind dynamic pressure and the interplanetary magnetic field (IMF) affecting dayside magnetic reconnection with Mercury's internal dipole field [e.g., *Killen et al.*, 2001; *Sarantos et al.*, 2007]. These two processes control the direct impact of solar wind plasma onto the surface and therefore the resultant sputtering of surface material, the most variable of the exospheric sources [e.g., *Sarantos et al.*, 2001, 2007; *Massetti et al.*, 2003; *Benna et al.*, 2010].

[4] Planetary ions are formed at Mercury through several processes, including photoionization of exospheric neutral atoms, sputtering directly off the surface by solar wind, and vaporization of micrometeoroids upon impact on the surface [*Cheng et al.*, 1987]. Once created, these planetary ions become part of the planet's plasma environment, and their motion is dominated by the interaction of the solar wind with Mercury's small internal magnetic field. The field is weak but sufficient to stand off the solar wind (under most circumstances) and form a small, permanent magnetosphere [*Ogilvie et al.*, 1974; *Slavin and Holzer*, 1979; *Russell et al.*, 1988; *Zurbuchen et al.*, 2004]. Mercury's magnetosphere has a basic structure that is similar to that of Earth but is much smaller, and Mercury's weaker internal field causes the planet to take up a much larger fractional volume [*Russell et al.*, 1988; *Slavin*, 2004]. Furthermore, Mercury's closer distance to the Sun places it in a region that subjects its magnetosphere to higher solar wind densities (by a factor of ~ 10 on average) and a more radial interplanetary magnetic field than at Earth. These factors together make Mercury's magnetosphere very dynamic, with reconnection rates ~ 10 times faster than at Earth and a Dungey cycle time of ~ 2 min [*Slavin et al.*, 2009]

compared with ~ 1 h at Earth [*Dungey*, 1961]. Mercury is therefore an important test case for our understanding of planetary magnetospheres and their interaction with the solar wind [*Baker et al.*, 2013].

[5] Mercury's small magnetosphere has a strong impact on fundamental plasma dynamics. Once created, ions begin to gyrate around the local magnetic field and are "picked up" into the convection of the magnetospheric plasma. Because heavy ions can have gyroradii that are large compared with the size of the small magnetospheric system, finite-gyroradius effects are expected to be prevalent, causing anisotropic or possibly nongyrotropic phase space distributions [*Delcourt et al.*, 2002, 2003]. In particular, both planetary ions and solar wind ions entering the open magnetosphere are expected to be in loss-cone distributions. Such distributions occur when ions with pitch angles inside the loss cone collide with the planet and are removed from the distribution. Finite-gyroradius effects can allow ions to be lost due to gyration across the magnetopause boundary and resulting pickup into the solar wind and give rise to nonadiabatic behavior, by which ions no longer gyrate around a single guiding center and can detach from magnetic field lines. Because gyroradius increases with the ratio of mass per charge (m/q), heavy ions of planetary origin (e.g., Na^+ ions, $m/q = 23$ amu/e) are expected to experience these effects markedly more than He^{2+} ($m/q = 2$ amu/e) from the solar wind.

[6] During its first Mercury flyby (M1) on 14 January 2008, the MErcury Surface, Space ENvironment, GEochemistry, and Ranging (MESSENGER) spacecraft [*Solomon et al.*, 2007] made the first observations of planetary ions with the Fast Imaging Plasma Spectrometer (FIPS) [*Zurbuchen et al.*, 1998; *Andrews et al.*, 2007]. MESSENGER flew by Mercury two additional times, on 6 October 2008 (M2) and 29 September 2009 (M3), before being inserted into orbit. A first analysis of M1 data revealed the presence of H^+ , He^{2+} , He^+ , Na^+/Mg^+ , and several other heavy ion species [*Zurbuchen et al.*, 2008].

[7] MESSENGER became the first spacecraft to orbit Mercury on 18 March 2011, and FIPS began taking continuous measurements shortly thereafter. Analysis of the first 65 d of orbital observations by *Zurbuchen et al.* [2011] reinforced the flyby analysis and revealed that planetary ions were typically organized into three dominant features. On the dayside, a large plasma population was observed at high northern latitudes, in the region of the magnetospheric cusp. On the nightside, plasma was observed near the equator, in the central plasma sheet. Finally, increased plasma flux was observed near the magnetopause with corresponding planetary ion enhancements that span the magnetopause boundary (as identified in magnetic field measurements [*Anderson et al.*, 2012; *Winslow et al.*, 2013]). These features are observed on nearly every orbit, despite highly variable solar wind and IMF conditions [*Gershman et al.*, 2012; *Baker et al.*, 2013].

[8] In this work, we present analysis of FIPS planetary ion measurements over the first three Mercury years of the MESSENGER orbital mission (25 March 2011 through 31 December 2011). Analysis results include ion composition, the distribution of different species in latitude and local time, their dependence on altitude, and their relative abundances in a variety of spatial domains. We have compared these results with the predictions of global modeling studies and

neutral exosphere observations. The results are shown to have important implications for planetary ion formation and transport in Mercury's small magnetosphere.

2. Description and Processing of Measurements

[9] The FIPS is a miniaturized time-of-flight (TOF) plasma mass spectrometer designed to measure heavy ions (atomic number > 4) in Mercury's space environment. When inside of the magnetosphere, the FIPS sensor measures energy per charge (E/q) from 0.1 to 13 keV/e, with a time resolution (scan time) of ~ 8 s. Outside of the magnetosphere, the E/q range is 0.05–13 keV/e and the time resolution is ~ 1 min. The instrument can resolve mass per charge from 1 to 60 amu e^{-1} . FIPS has a very large instantaneous field of view (FOV) of $\sim 1.4\pi$ sr and an approximate angular resolution of 15° . A portion of the FIPS FOV is blocked due to its position behind the spacecraft sunshade. A detailed description of the FIPS placement on the spacecraft, its FOV obstructions, and their impact on measured distribution functions was given by *Raines et al.* [2011]. Because the dominant flow in the magnetosphere is sunward or antisunward and the FIPS FOV points mostly to the side, the velocity distribution core (center) is typically not within the FOV. Under these conditions, we must apply a model-based recovery algorithm on an individual time-step basis to estimate plasma moments. Whenever the distribution is isotropic and hot (i.e., a thermal velocity comparable to convection speed), the plasma density and temperature can be estimated without knowledge of the three-dimensional bulk speed [*Raines et al.*, 2011]. Although these conditions are often reasonably met in both the magnetospheric cusp and plasma sheet, they do not apply to all of the measurements included in this large survey. Therefore, we do not attempt to recover the true number density of the ambient plasma from the observations in this work. We instead use observed number density, n_{obs} , as a proxy for comparisons of relative abundances of different ion constituents. Observed density is calculated by converting observed counts to phase space density then integrating over the observed velocity range, to reach particles per unit volume (cm^{-3}) observed by FIPS. *Gershman et al.* [2012] have described the calculation of n_{obs} for solar wind ions, but an identical calculation applies for both supersonic and subsonic plasmas. Observed density differs from the true number density of the ambient plasma by a time-dependent and unknown factor that depends on the vector flow velocity of the plasma, the plasma thermal velocity, and the orientation of the spacecraft. The assumption here is that different ions will have similar distribution functions to one another, and consequently their observed densities can be compared.

[10] If different ion species arrive at the instrument with substantially different velocity distribution functions, our estimates of relative abundances will be affected. For example, the heaviest planetary ions are likely to exhibit large loss cones. In the more extreme cases, ions that are created just before measurement may not have had sufficient time to scatter into an isotropic or even gyrotropic distribution and are thus highly directional. In contrast, solar wind ions, such as He^{2+} , are much more likely to be near equilibrium and have distributions that are not far from Maxwellian. The cusp is a region for which our estimates of relative

abundance are most trustworthy because the electric fields there are expected to be small and particles are not expected to be highly directional. Where the effects of the limited FOV of FIPS are substantial, observed densities for planetary ions reported here are lower limits.

[11] The FIPS uses a double-coincidence technique to greatly reduce background noise. However, spurious double-coincidence counts still do occur. These counts come from two main sources: the extension of very high count proton measurements into other times of flight, and the release of small numbers of ions from surface processes within the instrument. Although all major ion species reported here can be analyzed from the raw data, accuracy is markedly improved by removing these spurious counts. A detailed noise model and removal method has been developed and is employed with the data in this work at the individual scan level. After noise removal, ion species are identified from E/q –TOF tracks. To improve signal to noise, heavy planetary ions are grouped together into m/q ranges. This analysis makes use of two ion groups: O^+ group ($m/q = 16 - 20$ amu/e, including O^+ and water-group ions) and Na^+ group ($m/q = 21-30$ amu/e, including Na^+ , Mg^+ , and Si^+). Additional details concerning this process are given in Appendix 1.

[12] Observations analyzed here were taken on an orbit-by-orbit basis and thus occurred at altitudes ranging from 200 km to 15,248 km over 3.1 Mercury years (565 orbits). Because the MESSENGER orbital plane is approximately fixed in inertial space, the periaapsis of the orbit moves around the planet during each Mercury year. A side effect of this arrangement is that a particular local time of periaapsis is always sampled at the same part of Mercury's orbit around the Sun, so that local time variations in our figures may involve contributions from seasonal variations of the exosphere. Several sample orbits are shown in Figure 1, along with the respective Mercury true anomaly angle (TAA), which describes the position of Mercury in its orbit around the Sun, and the radial distance to the Sun (R).

[13] Another complication for the interpretation of these measurements arises from the placement of FIPS on one side of the spacecraft: measurements around the subsolar point are taken with FIPS pointing approximately perpendicular to the radial direction from Mercury. For these measurements, the angle between FIPS boresight vector and the Mercury radial direction is in the range 80° – 100° . In contrast, this angle is mostly in the range 40° – 60° for measurements elsewhere around the planet, symmetric about dawn and dusk. Small variations in pointing within the above ranges should not affect conclusions drawn from this analysis.

3. Data Analysis and Overview of Results

[14] We analyzed the detections of planetary ion species in the Na^+ group, the O^+ group, and He^+ , for data collected from 25 March 2011 through 31 December 2011, a span that includes the first 3.1 Mercury years of the MESSENGER orbital mission. We also included He^{2+} as a tracer for solar wind plasma, because these ions cannot be produced in substantial numbers within the Mercury environment. It is important to note that approximately 97% of the plasma ions measured by FIPS are protons, but because the focus of this work is planetary ions, protons are not included

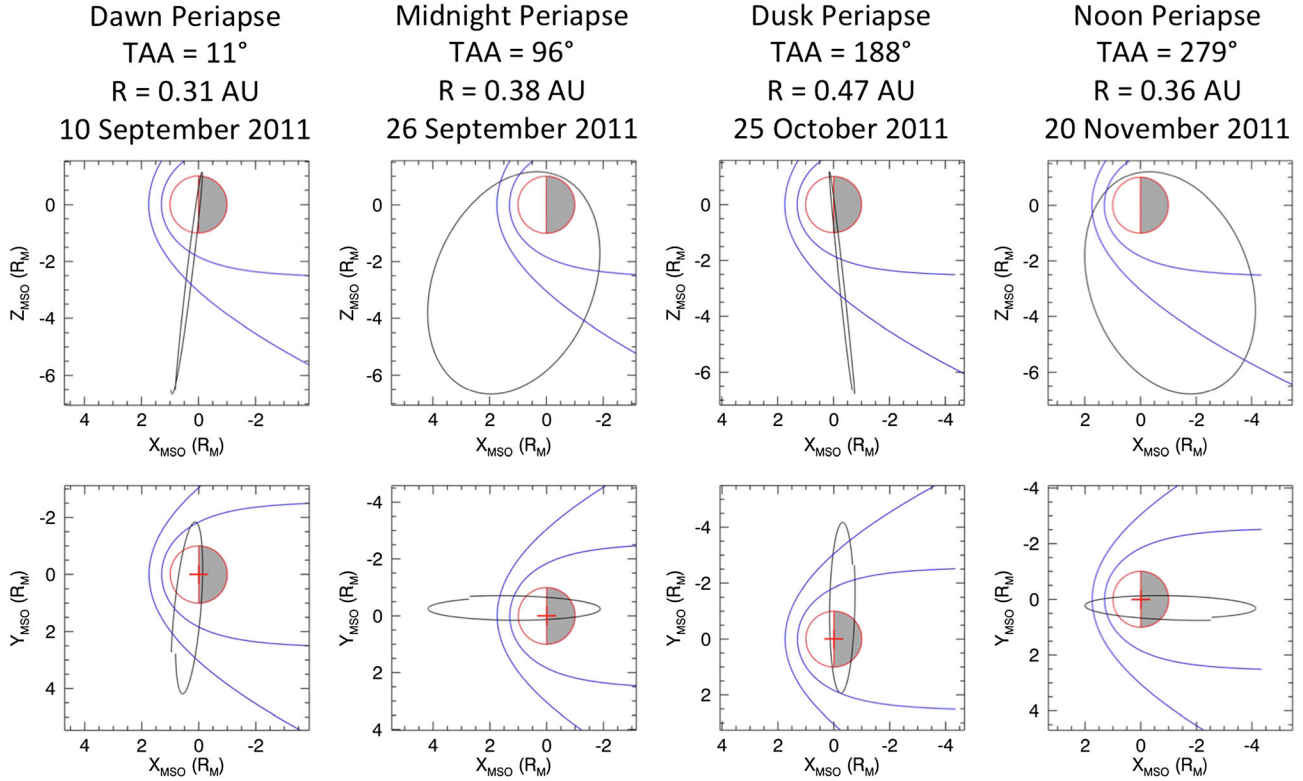


Figure 1. Selected MESSENGER orbits during the first three Mercury years of the MESSENGER orbital mission showing periaapsis at four different local times. Mercury TAA and radial distance to the Sun (in AU) are also given.

here. The average observed density for each of these species, and the ratio of each to the averaged n_{obs} for Na^+ -group ions, is given in Table 1. These values are computed by averaging the n_{obs} value from each FIPS E/q scan over all of the measurements, including all altitudes and latitudes. MESSENGER spends most of its time far from the surface, so lower n_{obs} values are weighted heavily in Table 1. The data from the first (M1) and second (M2) MESSENGER flybys of Mercury have been reanalyzed with these updated and refined techniques. They are also presented in Table 1.

3.1. Global Distribution of Measurements

[15] To assess the global spatial distribution of measurements, we co-added all measurements for all four species

over this period and binned them into two-dimensional spatial maps. The map for Na^+ -group ions is shown in Figure 2. The coordinate system used, Mercury solar orbital (MSO) coordinates, is centered on the planet and defined as follows: the X_{MSO} axis points from Mercury toward the Sun; the Z_{MSO} axis points north, normal to Mercury's ecliptic plane; and the Y_{MSO} axis completes the right-handed triad. The color in each cell represents average n_{obs} , calculated from the n_{obs} values measured within a $100 \text{ km} \times 100 \text{ km}$ grid divided by the number of FIPS scans taken within the cell, to normalize the inherently uneven sampling (in time) of the various spatial cells. The color scale for these and the other maps in this work is logarithmic to show variations on multiple scales. On these maps, black indicates $n_{\text{obs}} = 0 \text{ cm}^{-3}$, meaning that no counts were observed.

Table 1. Mean and Standard Deviation of Observed Density (in cm^{-3}), by Ionic Species, Averaged Over All Altitudes for Orbital and Flyby (M1 + M2) Measurements. The Ratio of the Mean to that of Na^+ -group Ions Is Also Given for Both Data Sets^a

Species	Orbital		M1 + M2	
	$\langle n_{\text{obs}} \rangle (\text{cm}^{-3})$	Ratio	$\langle n_{\text{obs}} \rangle (\text{cm}^{-3})$	Ratio
He^{2+}	$(3.9 \pm 0.0012) \times 10^{-2}$	7.7	$(1.0 \pm 0.012) \times 10^{-3}$	0.31
He^+	$(3.4 \pm 0.0035) \times 10^{-4}$	0.067	$(2.2 \pm 0.23) \times 10^{-3}$	0.68
O^+ group	$(8.0 \pm 0.010) \times 10^{-4}$	0.16	$(1.0 \pm 0.18) \times 10^{-3}$	0.31
Na^+ group	$(5.1 \pm 0.0043) \times 10^{-3}$	1	$(3.3 \pm 0.047) \times 10^{-3}$	1

^aObserved densities near the surface are at least one order of magnitude higher than given in this table. Standard deviation is divided by the square root of the number of measurements to estimate the error in the mean. Flyby data are from the magnetosphere only.

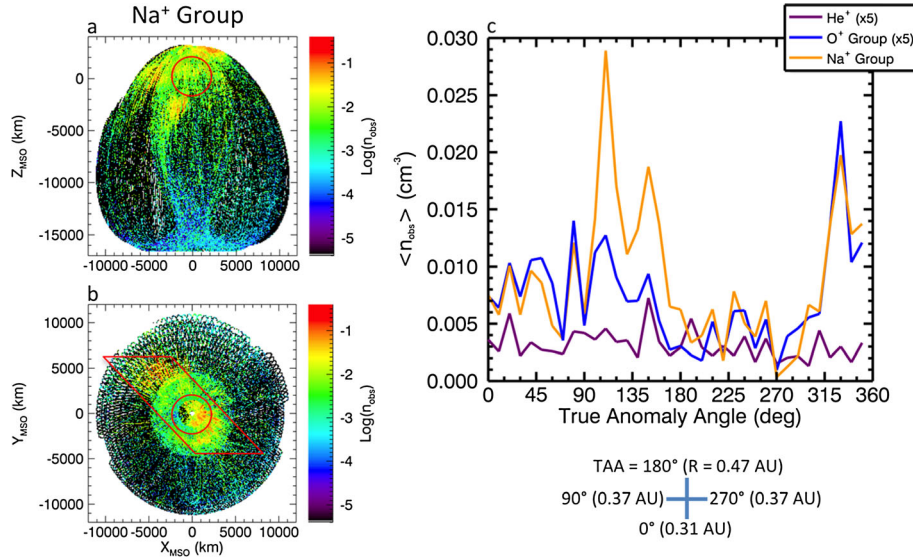


Figure 2. Average observed ion density (cm^{-3}) projected onto (a) noon-midnight and (b) equatorial planes. Binning within each plane shown is 100 km by 100 km. The Sun is to the right in these figures. Red circles show the approximate size of the planet in the projection planes. The approximate Mercury TAA at four MESSENGER periapsis local times (in the equatorial plane) is indicated in the legend at the bottom left, along with Mercury’s heliocentric distance in AU. The enhancements outlined in a red trapezoid are discussed in the text. (c) Average observed ion density (cm^{-3}) plotted versus Mercury TAA, collected into 10° bins for each of the three planetary species. Note that FIPS provides a local rather than a global measurement.

White indicates that the spacecraft did not pass through that cell.

[16] The noon-midnight projection in Figure 2a shows that planetary ions are much more abundant close to the planet, within ~ 5000 km, than they are farther away. Three areas of major enhancement Na^+ -group ions are clearly visible; these will be discussed below.

[17] The equatorial projection for Na^+ -group ions (Figure 2b) shows enhancements as well. In particular, enhancements centered on $(X_{\text{MSO}}, Y_{\text{MSO}}, Z_{\text{MSO}}) = (2500, -2000, 0)$ km on the dayside and $(-3500, 4500, 0)$ km on the nightside are very prominent. These observations may come from groups of orbits with an overall higher average observed density, a temporal effect. Alternatively, the dayside and nightside enhancements may be independent of one another and depend on the spatial region being sampled. If the enhancements are from groups of orbits, they would be those with MESSENGER periapsis at local times in the range 6–11.5 h (dawn-to-sub-solar sector). Orbits grouped together such as these are not likely to be entirely due to solar wind conditions, for three reasons: (1) Solar wind density and speed vary on much smaller timescales than the accumulated durations of these ~ 10 orbits [Gershman *et al.*, 2012; Baker *et al.*, 2013]. (2) Periods marked by a negative Z component of the IMF, $B_{Z,\text{IMF}}$, required for enhanced dayside reconnection and solar wind precipitation [Massetti *et al.*, 2003; Sarantos *et al.*, 2007] at the northern cusp, also vary on much smaller timescales [Baker *et al.*, 2013]. (3) Finally, the He^{2+} distribution (not shown) does not show obviously higher n_{obs} in these same orbits, as would be expected for this to be a solar wind effect. An examination

of the dependence of total observed density on Mercury TAA (below) sheds more light on these enhancements.

[18] These projections are a clear reminder that these measurements are made up of individual orbits and are actually quite sparse on the scale of Mercury’s space environment. This fact dictates many of the possible avenues for global analysis.

3.2. Variation With Mercury TAA

[19] The average observed density for each of the three planetary ions is plotted as a function of Mercury TAA in Figure 2c. Because the TAA changes by $\sim 5^\circ$ per day, measurements were collected into bins of 10° width to smooth the data. To facilitate comparison, the average observed densities for O^+ -group ions and He^+ were multiplied by a factor of 5.

[20] There are three prominent peaks for Na^+ -group ions, centered at TAA $\sim 110^\circ$, 150° , and 330° . These peaks show some qualitative similarities to peaks in neutral Na predicted by exospheric models [Leblanc and Johnson, 2010; Wang and Ip, 2011] and observed from Earth [Potter *et al.*, 2007]; this comparison is examined in detail in section 4.2. O^+ -group ions follow the same trends, at a nearly constant 20% fraction of the observed density of the Na^+ group through much of the Mercury year. The exception is for TAA 110° – 180° , for which O^+ -group ions are not strongly enhanced, unlike Na^+ -group ions. He^+ ions behave quite differently. Except for some very small enhancements, the clear peaks seen in Na^+ -group ions are absent. He^+ ions show a

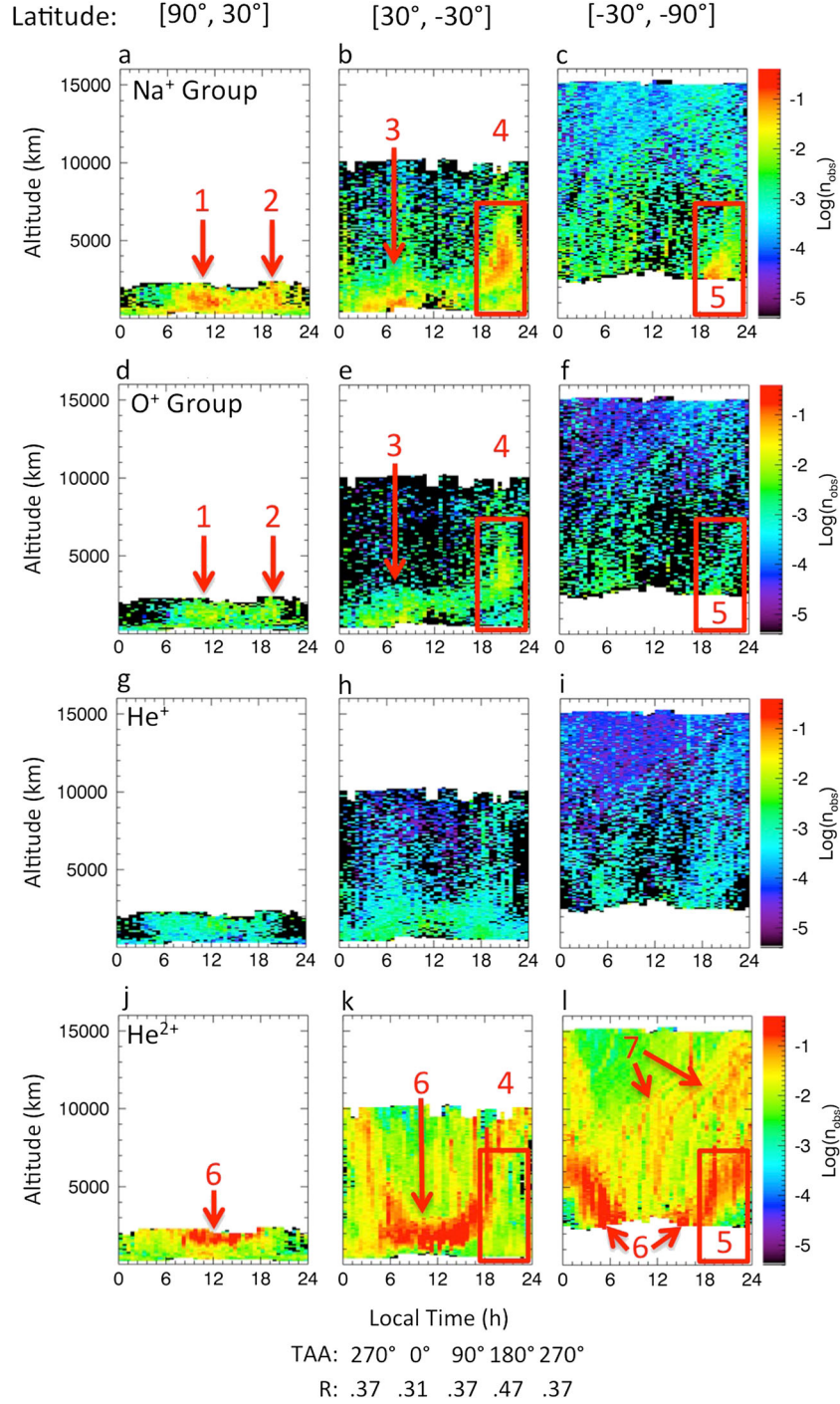


Figure 3. Average observed ion density (cm^{-3}) for all species as a function of altitude (km) and local time (h). Measurements are separated into three latitude ranges (inclusive). All ions are plotted on the same color scale, with the color bar for each panel showing the range present in that panel. Mercury TAA and heliocentric distance (R , in AU) are shown under Figure 3k and apply to all panels.

nearly constant average observed density throughout the Mercury year.

[21] When interpreting these results, one must remember that the local time of MESSENGER periapsis is locked to Mercury season and TAA. Therefore, each of the peaks in Figure 2c are from measurements taken at a particular local time of periapsis and Mercury–Sun distance. FIPS does not

provide an instantaneous global measurement. The spacecraft was at periapsis for local times in the 19–20.5 h range for the peaks at TAA $\sim 110^\circ$ and 150° , when Mercury was approaching its aphelion of 0.47 AU from the Sun. For the TAA $\sim 330^\circ$ peak, MESSENGER periapsis was at local times in the range 6.5–11 h (Figure 2b) and moving away from its perihelion of 0.31 AU. The predicted peak in

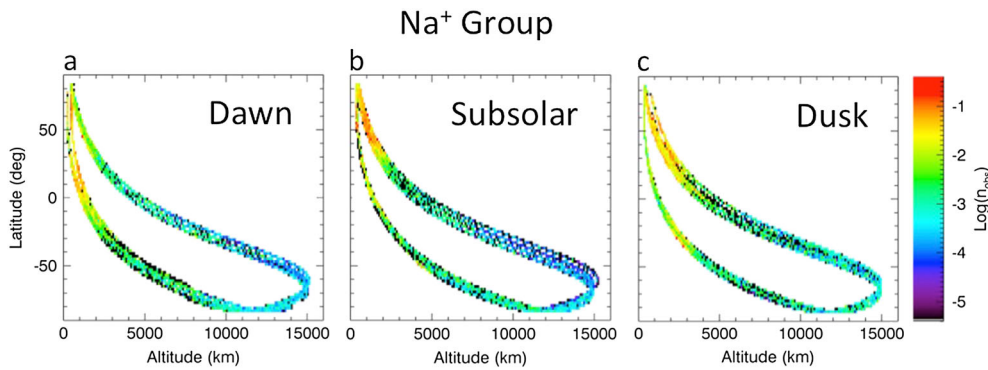


Figure 4. Altitude profiles of Na^+ -group ions obtained from summed orbits. Observed density is binned by latitude (0.5° bin widths) and altitude (100 km bin widths) and averaged, analogous to Figure 2. See text for further details. These figures show the interconnection of latitude and altitude resulting from MESSENGER's highly eccentric orbit.

exosphere content at aphelion, at TAA = 180° [Leblanc and Johnson, 2010], coincided with a time when MESSENGER was above the dusk terminator. In principle, then, it is impossible to attribute conclusively the enhancements in Figure 2c to seasonal variations. We will return to this question below.

3.3. Variation With Altitude and Local Time

[22] A major source of ions measured by FIPS is expected to be photoionization of exospheric neutral atoms. This process takes place at all altitudes and without regard for magnetic boundaries, depending mainly on the neutral atom generation and convection processes. Therefore, in sunlight the observed density of ions is expected to show a strong dependence on altitude. Once formed, ions are also subject to the magnetic and electric field forces in the environment, which complicates analysis of altitude profiles. In eclipses, of course, no photoionization takes place, making electromagnetic forces the primary sources of influence.

[23] An overview of the dependence of average observed density on local time and altitude for the four ion species considered in this study is shown in Figure 3. These maps were created by binning the observations by altitude (100 km bin width) and local time (0.5 h bin width) and further separated into 60° latitude ranges, with the same normalization and color scheme as for Figures 2a and 2b. These maps show a variety of enhancements and a general altitude profile that is different for each ion species. Altitude profiles will be discussed in more detail in section 3.2.1.

[24] The Na^+ -group ions show an enhancement at high latitudes (Figure 3a, feature 1), centered at local time ~ 10.5 h, which corresponds, at least in part, to the northern magnetospheric cusp. An additional enhancement is centered at local time ~ 19 h (Figure 3a, feature 2). Around the equator (Figure 3b), an enhancement is evident around the dawn terminator (local time 6, feature 3), consistent with some neutral and ion transport models (see section 4.2 below). Another enhancement is located in the premidnight sector (local time ~ 20 h), at altitudes above ~ 2000 km, similar to the one evident in Figure 3a, feature 2. This latter enhancement extends to low latitudes (Figure 3c, feature 5) to an altitude of ~ 6000 km. Slices through the Cartesian binning of the data (similar to Figures 2a and 2b, not shown) confirm that these three enhancements (features 2, 4, and 5

in Figure 3) appear to be part of a single feature that creates a large asymmetry between dawn and dusk.

[25] The O^+ -group ions (Figures 3d, 3e, and 3f) show the same major features (features 1–5), at lower average observed density, as the Na^+ -group ions (Figures 3a, 3b, and 3c). Close comparison between the two groups reveals that in some cases even the small-scale structure is reproduced (features 2, 3, and 4). In other cases, only the large-scale structure is similar, with cells of particular high or low n_{obs} arranged a little differently (features 1 and 5). These differences may arise from the limited statistics for the low-abundance O^+ -group ions and need not represent a global difference in the behavior of the two ion groups.

[26] The most obvious feature of the He^{2+} map is the magnetosheath, visible as thick, nearly solid red bands (Figures 3j, 3k, and 3l, feature 6). Orbits with overall higher n_{obs} measurements are also evident, as narrow, right-turning trails (Figure 3l, feature 7). With these observations to guide the eye, it is possible to see some enhancements in the other ions at the same locations as those for He^{2+} . Features 4 and 5 from Figure 3 are also identified in Figures 4k and 3l, showing that these enhancements only partially overlap the magnetosheath. This enhancement may be related to the magnetopause-associated heavy ions that are commonly seen in individual passes through the magnetosphere [Zurbuchen et al., 2011].

[27] He^+ ion maps do not show the same clear enhancements as the Na^+ -group ions, but instead they are much more evenly distributed around the planet. The average observed density spans only two orders of magnitude, 10^{-4} to 10^{-2} cm^{-3} , rather than the five orders of magnitude spanned by Na^+ -group ions. Low-altitude enhancements are present, but they are much less pronounced than for the Na^+ -group and O^+ -group ions. These patterns likely indicate a different source for He^+ than for Na^+ -group and O^+ -group ions. One possible source is charge exchange between solar wind He^{2+} and exospheric neutrals, gravitationally bound and/or escaping. If this mechanism were a dominant source, then charge exchange would be most prevalent where He^{2+} density is the highest—in the magnetosheath region. Comparison of Figures 3h to 3k and Figures 3i to 3l suggests that unlike other planetary ions, slight enhancements in the He^+ distribution may be present in the magnetosheath (bright red bands in Figures 3k and 3l).

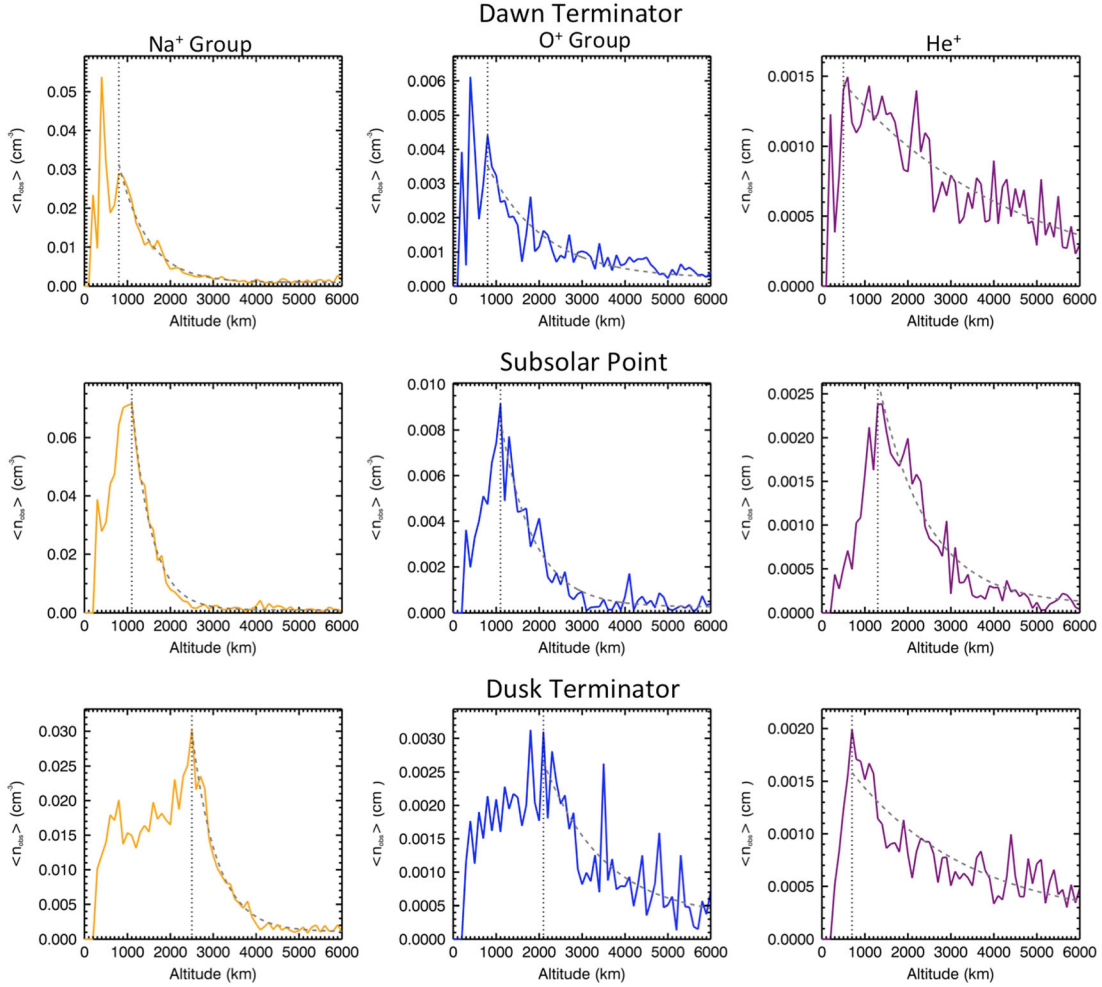


Figure 5. Altitude dependence of observed density in sunlight, over all latitudes, for three species in three regions of local time. The vertical dotted line denotes h_0 from Table 2. The exponential curve generated from the corresponding B value (Table 2) is also shown (dashed curve).

[28] Because of differences between measurements in sunlight and eclipse, we consider the two sets of measurements separately in the quantitative analyses in the next two sections. The eclipsed region is defined as measurements taken when the spacecraft was in the shadow within $1 R_M$ perpendicular distance of the $-X_{\text{MSO}}$ axis. Everywhere else is considered sunlit.

3.3.1. Ion e -Folding Heights

[29] In sunlight, we can quantify the altitude dependence of Na^+ -group, O^+ -group, and He^+ ions by estimating an e -folding height. We intentionally avoid the use of the term “scale height” to emphasize that this quantification is only mathematical in nature and is independent of any physical interpretation. Because these altitude profiles are fit reasonably well by an exponential function, e -folding height provides a useful metric for comparison.

[30] We subdivided the observed density for each of these three species into 3 h regions of local time, centered on the dawn terminator (local time 6 ± 1.5 h), subsolar point (local time 12 ± 1.5 h), and dusk terminator (local time 18 ± 1.5 h). The orbits in each of these ranges, summed and plotted versus latitude in Figure 4, show the close coupling of altitude

and latitude due to MESSENGER’s highly eccentric orbit. Observed density was then summed over latitude, to produce profiles of observed density versus altitude alone (Figure 5). These altitude profiles show clear differences among species and local time regions.

[31] We fit the dependence on altitude (h) of the observed density (n_{obs}) to a function of the form:

$$n_{\text{obs}} = A \exp[-(h - h_0)/B] + C \quad (1)$$

where A , B , and C are determined by a least-squares fit to the data. The peak altitude (h_0) denotes the portion of the data we chose to fit; it is the altitude at which the observed density starts to fall off clearly with altitude. The B parameter represents the e -folding height of the ions, the height at which the observed density has decreased by $1/e$ of the value at h_0 . (The C parameter, which is very small, has negligible influence on the e -folding height.) To estimate the uncertainty in these fits, we used a bootstrap method [Hesterberg *et al.*, 2010; Hesterberg, 2011] as follows: We produced 1000 bootstrap samples of the altitude profile by randomly

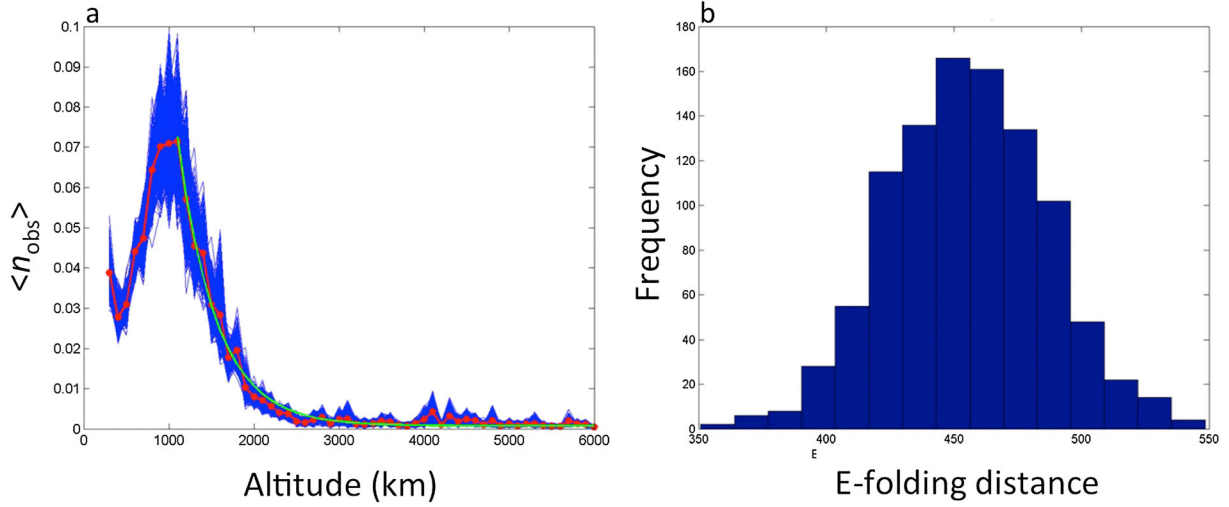


Figure 6. Estimation of e -folding distance error for Na^+ over the subsolar region. (a) Comparison of 1000 curves constructed from chosen bootstrapped samples of data in 100 km altitude bins (blue) with the average curve (red). (b) Distribution of e -folding distances derived from exponential fits to each of the curves in (a), from which the average e -folding distance was computed. The curve produced from that average e -folding distance is shown in green in Figure 6a.

sampling with replacement from the measurements within each 100 km wide bin. The distribution with altitude of the binned means in each bootstrapped sample was fit with the exponential function (Figure 6a) to produce a distribution of e -folding distances that reflect the expected sampling variability (Figure 6b). The h_0 and average B values are the most physically relevant and are tabulated in Table 2. To facilitate comparison across local times, the B values at dawn and dusk are divided by B at the subsolar point for a given ion species. These values are shown in parentheses in Table 2.

[32] For the Na^+ group, the e -folding height shows a clear dependence on local time, with a much smaller B in the subsolar region than at the terminators. This pattern is consistent with the expected behavior of neutral Na, as the result of increased radiation pressure at the subsolar point [Mura *et al.*, 2007]. O^+ -group and He^+ -ions show the same smaller e -folding height at the subsolar point than the terminator regions. He^+ ions are much more extended than the other two groups, and their measured distribution is substantially more extended at the dawn terminator. The implications of these differences are discussed in section 4.

[33] The quantity h_0 denotes the altitude above which an e -folding scale height can be well defined. The h_0 values for Na^+ -group and O^+ -group ions gradually increase from dawn to subsolar to dusk, whereas He^+ ions do not show this trend. This behavior for the heavy ions does not appear to be an effect of the FIPS pointing and its limited FOV. The angle between FIPS boresight vector and the nadir direction can be used to generally assess pointing as a function of altitude and local time. Although there are differences in this angle between the dawn and dusk regions, it stays within 75° , so that the planet is within the FOV most of the time in both regions. Seasonal variations may play a role: The dusk-side observations are taken when Mercury's heliocentric distance is near maximum (0.47 AU), whereas it is near minimum (0.31 AU) for the dawn and subsolar measurements.

3.3.2. Composition Dependence on Local Time

[34] To extend quantitatively the comparison of composition in the dusk terminator, subsolar, and dawn terminator regions, the average observed density in each was calculated and plotted (Figure 7). In Figure 7a, data only from $\pm 30^\circ\text{N}$ latitude were used. In Figure 7b, these averages were

Table 2. Peak Altitude (h_0 , km) and e -Folding Distance (B , km) From Fits of Average Observed Density Versus Altitude at Three Local Times^a

Local Time		Na^+ Group	O^+ Group	He^+
Dawn	B	670 ± 40 (1.5)	1330 ± 250 (1.8)	4040 ± 300 (3.6)
	h_0	800	800	500
Subsolar	B	460 ± 30 (1)	760 ± 70 (1)	1140 ± 90 (1)
	h_0	1100	1100	1300
Dusk	B	580 ± 40 (1.3)	1400 ± 300 (1.8)	2790 ± 350 (2.6)
	h_0	2500	2100	700

^aValues in parentheses are ratios to the e -folding distance at the subsolar point for a given ion. h_0 is the altitude above which these e -folding distances were obtained.

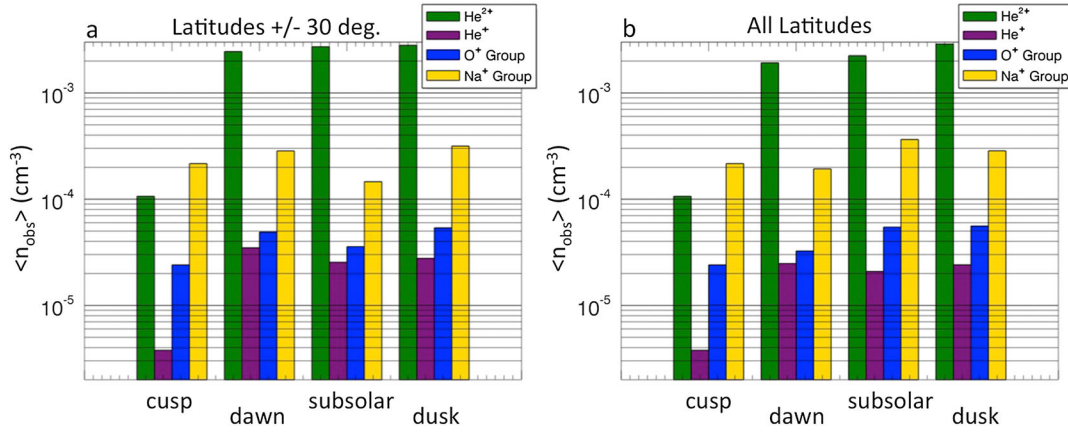


Figure 7. Ion composition on Mercury's dayside for two latitude ranges. Shown are n_{obs} averaged over all measurements, including all altitudes and the indicated range of latitudes and local times. The cusp observations are the same in both panels. Statistical errors in these averages are $<1\%$.

obtained from data at all latitudes. All altitudes were included in both panels. The average observed densities from the cusp region, defined broadly here as 6–18 h and 45°–90° latitude, was added to both panels for comparison. The statistical errors in these averages are $<1\%$.

[35] The most interesting feature of the cusp composition is that the average observed density of Na⁺-group ions in the cusp exceeds that of He²⁺ by a factor of ~ 2 . (Even though observed density for Na⁺-group ions exceeds that of the solar wind tracer, He²⁺, protons are still the dominant plasma in the cusp during most, if not all, orbits.) It may be possible to use this very high ratio of Na⁺-group to He²⁺ ions as a compositional marker for cusp plasma. If so, then tracking of plasma convection from the cusp to other regions of the magnetosphere might be enabled. Of course, this large ratio would need to be verified by examining a large number of individual orbits.

[36] Around the equator ($\pm 30^\circ$ latitude, Figure 7a), the average observed density for all ion groups is depressed at the subsolar point, the same trend observed in B values above. For Na⁺-group ions, the subsolar n_{obs} is 49% of the average of the dawn and dusk values. O⁺-group and He⁺ n_{obs} values are depressed less, with subsolar averages that are 69% and 81% of their respective dawn-dusk averages. This effect is inverted for Na⁺ and O⁺ groups when all latitudes are included: The n_{obs} values at subsolar local times, which include the large plasma source of the cusp, are enhanced relative to the dawn and dusk regions.

[37] For observations during eclipse, a fairly small fraction, we focus on measurements in and around the central plasma sheet, within 750 km of the geographic equator. This volume includes the magnetic equator, which is shifted north of the geographic equator by ~ 500 km [Anderson et al., 2011]. These plasma sheet observations were further subdivided into premidnight, occurring between local times of ~ 21 and 0 h (midnight), and postmidnight, occurring between local times of 0 and ~ 3 h. (The precise local time bounds are determined by the eclipse condition, described above.) Because of MESSENGER's orbit, these restrictions produce observations that lie entirely within two narrow altitude bands, each about 1000 km thick, and centered at altitudes

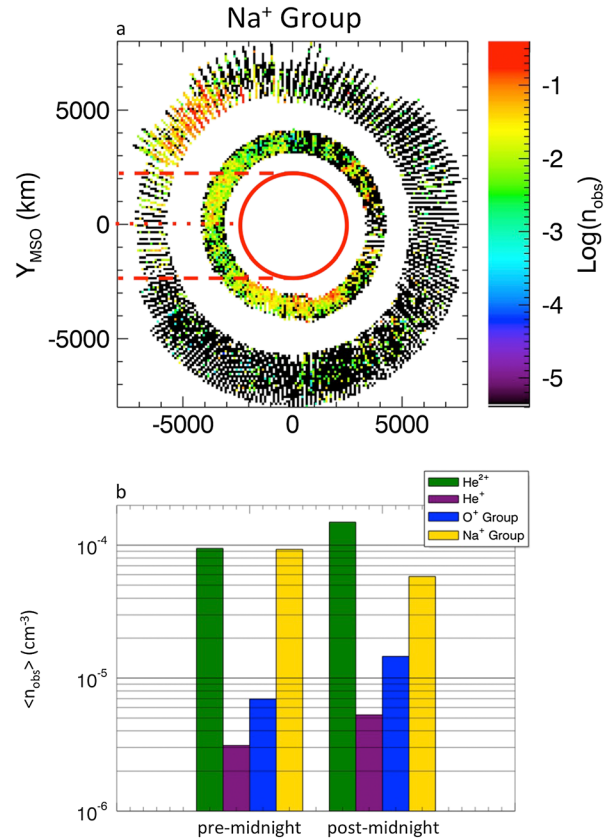


Figure 8. (a) Equatorial cross-section of average observed density, from observations within 750 km of the geographic equator. Measurements are normalized by the number of FIPS scans within each $100 \text{ km} \times 100 \text{ km}$ bin, as in Figure 2. Statistical errors are $<1\%$. A red circle shows the approximate size of Mercury in the equatorial plane. The Sun is to the right. (b) Average observed density on the nightside, including only measurements from Figure 8a that were collected while MESSENGER was in the shadow of Mercury, delineated by dashed red lines. A dotted red line separates the (top) premidnight sector from the (bottom) postmidnight sector within the shadow.

of ~600 km and ~3600 km (Figure 8a). These bands are too restricted to be used to analyze the functional dependence of observed density on altitude. The average n_{obs} values for Na⁺-group ions, O⁺-group ions, He⁺, and He²⁺ were each summed for all measurements within these two regions. The results are displayed in Figure 8b.

[38] The main result is a persistent enhancement in Na⁺-group ions by a factor of 1.6 in the premidnight sector compared with the postmidnight sector. This enhancement is visible in both the inner and outer ring in Figure 8a. The enhancement around the dawn terminator, seen in Figure 3, is also apparent. On the contrary, none of the other ion species show this enhancement. We will return to these results in section 4.6.

4. Discussion and Implications

[39] The observations presented in this paper provide a fresh perspective on previous studies of ions and neutral atoms in Mercury's environment. There are inherent similarities and differences expected between these two populations. The neutral exosphere is likely the major source of ions at Mercury, so if measured soon after ionization the ions may retain some characteristics of the neutral atom population, such as spatial distribution. Yet because ions and neutrals are controlled by different forces, ions measured long after ionization will show a much less direct relationship to the population of neutrals. In making these comparisons, our aim is to begin to differentiate between these two situations.

4.1. Overall Composition

[40] It is clear that the Na⁺ group dominates the planetary ions (Table 1), consistent with expectations from ground observations and photoionization rates [Killen *et al.*, 2007] and previously reported measurements at Mercury [Zurbuchen *et al.*, 2008, 2011]. As discussed in the Appendix, the average density measured in this group likely comes from a combination of Na⁺ and Mg⁺ ions, produced both by photoionization of exospheric neutrals and sputtering of the surface. Production rates of Mg⁺ from the exosphere should be much less than that of Na⁺ if neutral Mg densities inferred from the second flyby data are representative [Sarantos *et al.*, 2011], but the relative effect of surface-generated ions on our measurements is difficult to estimate at present. Average observed densities for Na⁺-group and O⁺-group ions obtained during the flybys are quite comparable to orbital values, within the larger statistical uncertainty resulting from poorer counting statistics. He⁺ and He²⁺ measured during the flybys, in contrast, are much different from their orbital averages. Flyby averages were taken from magnetospheric data only, which likely accounts for a substantial drop in He²⁺. However, He⁺ actually had a larger average observed density during the flybys than found in the orbital data. The flyby trajectories were much different from MESSENGER's orbit, because the spacecraft passed from deep in the magnetotail in premidnight, past the dawn terminator close to the planet, to the dayside. The deep tail observations obtained during M1 and M2 are not matched in the orbital data, and it is possible that this different sampling contributed to the observed differences in He⁺.

4.2. Variation With TAA

[41] We return to the variation of observed ions with TAA in Na⁺-group ions (Figure 2). *Leblanc and Johnson* [2010] modeled the total Na content of the Mercury exosphere through a full Mercury year, adjusting the contributions of the various production processes to explore their effects. They then calculated Na brightness and compared that prediction with trends versus TAA from ground-based observations. They predicted a factor of 3 variation in exospheric Na content as a function of Mercury true anomaly, with minima of 1.5×10^{28} Na atoms at TAA = 140° and 70° and maxima of 4.5×10^{28} Na atoms at TAA = 180° and 0° (their Figure 12). Their Figure 11 shows that the peak at TAA = 180° is due to the dominance of photon-stimulated desorption and solar wind sputtering, whereas thermal desorption is the dominant process producing the peak at TAA = 0°.

[42] If we consider the two Na⁺-group ion peaks (which are very close to one another) as representing one peak at ~130°, then FIPS ion measurements show two peaks separated by ~200°. This separation is within 10% of that predicted by *Leblanc and Johnson* [2010]. Clearly, their modeling results do not fully explain observed differences in Na⁺-group distribution reported here. For example, in sunlight, a large enhancement is seen only on the dawn side, for TAA = 0°, whereas the modeling predicts enhancements on the dusk side (TAA = 180°) as well. In general, their results show peaks centered at TAA = 40° and TAA = 300°, although results from different specific models showed substantial variations.

[43] Variation of Na D₂ emission with TAA was reported from ground observations by *Potter et al.* [2007]. Their Figure 1 shows a two-peak structure, in which the first peak is split, a pattern qualitatively similar to FIPS observations (Figure 2c), except that the TAA values for the peaks are shifted. As shown by *Potter et al.* [2007], these peaks are centered at TAA ~ 70° and TAA ~ 300°, whereas the peaks in the FIPS measurements are at TAA ~ 130° and TAA ~ 330°. *Potter et al.* [2007] offered that radiation acceleration has a varying effect on this emission over a Mercury year, and so emission does not relate directly to column abundance of Na. They normalized their emission data to one set of conditions. Their Figure 2 shows Na emissions that should be directly related to column abundance. These normalized emissions do not compare well with FIPS observations (Figure 2c), however. *Wang and Ip* [2011] modeled these Na D₂ emissions and found total Na emission peaks at TAA = 90° and 310°. Their study did not involve calculation of Na content, which differs from emission by a TAA-dependent radiation acceleration term. Nonetheless, it is interesting to note that their results show two peaks separated by ~220°, which is also within 10% of the 200° separation of the peaks in FIPS Na⁺-group ions.

4.3. Dayside Planetary Ion distribution

[44] *Delcourt et al.* [2003] modeled Na⁺ in Mercury's magnetosphere with a simplified version of the exosphere model of *Leblanc et al.* [2003] and analytic expressions for the magnetic and electric fields. Na⁺ particles were launched from a variety of locations and with a variety of energies, then flown through the model magnetosphere by integrating

the full equations of motion. Their results show that the dayside magnetosphere, local time $\sim 8\text{--}16$ h, is populated with very low energy ions having energies < 100 eV. During the orbital observations reported in this study, FIPS was operated with two minimum energies: 100 eV in burst mode (8 s time resolution) and 46 eV in normal mode (64 s time resolution). Typically, FIPS was in burst mode on the dayside, within a few R_M of the surface. It is possible that this 100 eV energy threshold near the planet could partially account for the generally lower average n_{obs} values at the subsolar point. If ions were present, they may have been below the FIPS energy threshold and thus unable to be measured. In February 2012, the FIPS burst-mode energy threshold was lowered to 46 eV. Analysis of these data, outside the range considered in this study, should provide fresh information on this point.

[45] Other features of the FIPS-derived ion spatial distributions correlate with previously published results or predictions for Na neutrals. Some exospheric simulations predict a dawn enhancement of neutral sodium [Leblanc *et al.*, 2003; Misawa *et al.*, 2008; Leblanc and Johnson, 2010]. Yagi *et al.* [2010] carried out simulations in which Na^+ test particles were tracked through electric and magnetic fields derived from a magnetohydrodynamic model, using the same exospheric model as that of Delcourt *et al.* [2003]. They studied Na^+ behavior under four distinct sets of solar wind conditions. In all cases, their simulations showed enhancement of Na^+ density in the morning sector, over the local time range 6–12 h. As seen in Figure 2c, FIPS results show a peak in Na^+ -group and O^+ -group ions when MESSENGER periapsis was in this local time range. (The local time ranges in Figure 7 are not conducive to observing this enhancement.). The fact that average observed density for Na^+ group ions in the cusp exceeds that of He^{2+} is consistent with the cusp serving as a major source of planetary ions due to increased surface exposure to solar wind sputtering [e.g., Massetti *et al.*, 2003; Sarantos *et al.*, 2007; Benna *et al.*, 2010]. The cusp is a strong source of planetary ions, as evident in these measurements, and may also serve to trap planetary ions that are created from escaping neutrals in the magnetosheath.

4.4. Altitude Dependence

[46] The functional fits of observed dependence on altitude yield many differences and reflect a combination of competing effects. First, escape of neutrals from Mercury's gravity under the influence of radiation pressure yields a neutral density that peaks at the surface and then generally drops off as the inverse of altitude. Because Mercury's exosphere is considered optically thin above ~ 50 km altitude, the number of photons is constant with altitude. Therefore, the production of ions by photoionization is simply proportional to neutral density. If these ions are measured close to the time that they are created by photoionization, they could serve as a tracer for the neutral atom density. However, as the time between photoionization and measurement increases, the influence of plasma processes increases as well. One way to separate these two regimes would be to limit the altitude consideration to low altitudes (< 2000 km) at which the effects of convection

should be minimal. However, the observed flux typically peaks near this altitude and begins to fall off at higher altitudes.

[47] One option for the interpretation of the e -folding distance is as a scale height, as is done for gravitationally bound exospheric neutral atoms. For neutral species, scale height reflects the ratio of particle mean energy to the potential in which the particles find themselves, which includes only gravity in the simplest scenario:

$$H = \frac{kT}{mg} \quad (2)$$

where k is Boltzmann's constant, m is particle mass, and g is gravitational acceleration. The scale heights of various exospheric components at the same "temperature" T (i.e., mean ejection velocity from the surface) are therefore different by the ratio of their masses. Thus, comparing Hm gives information about the temperature of the neutral populations. Interpreting the ion e -folding distances calculated in this work as scale heights raises several issues. Even at 1000 km, the altitude at which observed density typically peaks, a Na^+ ion has the gravitational potential energy of ~ 2.4 eV. When compared with the high average energy measured for the ions ($\sim 2\text{--}4$ keV), gravity is negligible. Furthermore, measured He^+ exhibits very large e -folding heights, whereas the He neutral atoms are expected to be accommodated to Mercury's surface temperature, ~ 700 K. The variation of e -folding heights among species is more likely related to variation in the ratio of ion gyroradius to neutral scale height [Hartle *et al.*, 2011].

[48] These results can also be interpreted in the context of average magnetospheric boundary locations. From a statistical analysis of MESSENGER Magnetometer observations, Winslow *et al.* [2013] showed that the average altitude of the subsolar magnetopause is 1100 km, and the maximum altitude is 1340 km. Those authors also found that the average altitude for the subsolar bow shock is 2340 km, and the maximum altitude is 2660 km. In the subsolar region, FIPS measurements show peaks in n_{obs} in the range of the Winslow *et al.* [2013] magnetopause locations. This agreement is consistent with expectations, in that planetary ions formed from neutrals upstream will tend to collect at the subsolar magnetopause where plasma flow velocity is low [Spreiter *et al.*, 1966]. Moreover, planetary ions that form in the dayside magnetosphere or flow into that region will tend to gyrate across the magnetopause and out of the magnetosphere because of their large gyroradii. This effect should be most pronounced in the subsolar region, where the distance from the surface to the magnetopause is at a minimum.

[49] Interpretation of these differences is further complicated by the possibility that different species are present with substantially different distribution functions. In the simplest case, consider He^+ ions that are much hotter than Na^+ -group ions. Such a scenario might follow from the much larger e -folding distance for He^+ . In such a case, He^+ would be more easily measured by FIPS with its limited FOV, especially at larger convection speeds that might be present at larger altitudes.

4.5. Source of He^+

[50] The measurements reported here show that He^+ is distributed differently from the other two planetary ion groups

observed in abundance at Mercury, the O⁺-group and Na⁺-group ions. He⁺ at Mercury may be created by charge exchange between He²⁺ and any neutral atom or by ionization of exospheric He from the surface. He⁺ created by charge exchange should show enhancements where He²⁺ density is the highest—in the magnetosheath. Although some enhancements in He⁺ are visible in this area (Figures 3h and 3i), there is only partial correlation with magnetosheath enhancements in He²⁺ (Figures 3j, 3k, and 3l). The even distribution of He⁺ is consistent with the distribution of a He exosphere given by several models [e.g., *Hartle and Thomas, 1974; Hartle et al., 1975; Leblanc and Chaufray, 2011*]. Thus, the distribution of He⁺ in the FIPS measurements presented here qualitatively supports ionization of exospheric neutral He as the more important source for He⁺ than charge exchange. However, the ultimate source of He in those models is from surface implantation by the solar wind. In that light, the fact that He⁺ is depleted in the cusp measurements, contrary to the other two planetary ion groups, requires further explanation.

4.6. Nightside Distribution of Na⁺-group Ions

[51] As described above, the nightside (eclipse) measurements show the interesting result that the Na⁺-group flux is higher on the premidnight side than on the postmidnight side (Figure 8). MESSENGER periapsis was in the premidnight sector for Mercury TAA = 100° to 140° (Figure 2c). The premidnight sector is where we expect to find Na⁺ ions moving under the influence of gradient-curvature drift, the velocity imparted clockwise around the planet (when looking down from north) by the combined effects of magnetic field gradient and curvature. However, high magnetic field gradients make pure drift motion unlikely around the magnetic equator and in the central plasma sheet [*Lukyanov et al., 2001*], where the premidnight enhancement is most prominent.

[52] As discussed above, *Yagi et al. [2010]* simulated Na⁺ behavior within Mercury's magnetosphere under four distinct sets of solar wind conditions. In all cases, Na⁺ was found to be enhanced from local time ~1 to 11 h. Direct comparison of their results with FIPS observations is complicated by the fact that solar wind and IMF conditions encountered by MESSENGER varied over a wide range [*Baker et al., 2013*]. However, it is safe to conclude that, because the model results never showed an enhancement on the premidnight side, the model results do not show the same behavior as the observations in this regard. One reason may be the fact that the bulk of Na⁺ energies were below 5 keV in the model, whereas FIPS observed substantial fractions of the Na⁺-group population with energies up to 10 keV.

[53] *Delcourt et al. [2003]* found that Na⁺ ions launched from the region of the northern cusp were substantially energized (up to 10 keV) and precipitated on the premidnight side of the planet, unless their gyromotion took them out of the magnetosphere first. These authors credited this behavior to nonadiabatic motion, driven largely by the small size of Mercury's magnetosphere and the large Na⁺ gyroradius. These results qualitatively match the observations described in this work, particularly the enhancement in observed density of Na⁺-group ions on the premidnight side in eclipse. These FIPS measurements may constitute the first

observational evidence of large-scale nonadiabatic motion of heavy ion particles in Mercury's magnetosphere.

[54] We recall here that only Na⁺-group ions show the premidnight enhancement in eclipse; the other ion species do not (Figure 8a). Nonadiabatic motion depends on gyroradius, which increases with m/q . The gyroradius of Na⁺-group ions is nearly 50% larger than that of O⁺-group ions (and much larger than He⁺ and He²⁺). This difference may be enough to account for the difference in behavior.

5. Summary and Conclusions

[55] In this work, we have presented an overview of ion measurements made by the FIPS sensor during the first three Mercury years of MESSENGER orbital observations, from 25 March 2011 through 31 December 2011. We used two-dimensional spatial maps, functional fits, and regional averaging of observed densities as the main tools in this analysis. We have provided the first comprehensive overview of the heavy ion composition at Mercury and, where possible, drawn connections to previously published observations, models, and physical explanations.

[56] We find the following:

[57] (1) He²⁺ ions are the second most abundant ion (after protons), with an average observed density of $3.9 \times 10^{-2} \text{ cm}^{-3}$. Na⁺-group ions are the next most abundant, with an average observed density of $5.1 \times 10^{-3} \text{ cm}^{-3}$, followed by O⁺-group ions ($8.0 \times 10^{-4} \text{ cm}^{-3}$) and He⁺ ($3.4 \times 10^{-4} \text{ cm}^{-3}$).

[58] (2) The average observed density of Na⁺-group ions exceeds that of He²⁺ in the northern magnetospheric cusp by a factor of ~2. This ratio may be a compositional marker of the cusp.

[59] (3) Within 30° of the equator and in sunlight, all planetary ions show minimum observed densities at the subsolar point. Near the equator, the average observed density of Na⁺-group ions is reduced to 49% of the terminator value. Reductions are less for other species.

[60] (4) All three planetary ion species considered show a different dependence on altitude and some differences with local time. Na⁺-group ions fall off most strongly with altitude, followed by O⁺-group ions and then He⁺.

[61] (5) In eclipse, Na⁺-group ions are enhanced in the premidnight sector. Such an enhancement is consistent with modeling of Na⁺ energization and transport by *Delcourt et al. [2003]*. This pattern may be observational evidence that nonadiabatic effects are important in Mercury's magnetosphere on a large scale.

[62] These results provide the first quantitative assessment of plasma composition at Mercury, its spatial variations, and temporal variations over an entire Mercury year. They give important clues to understanding exospheric and magnetospheric processes on the innermost planet.

Appendix A: Ion Identification From E/q and TOF

[63] After background removal, the next step in the detailed analysis of FIPS data is the assignment of individual counts to a particular ionic species. Because FIPS measures time of flight rather than m/q directly, this step is

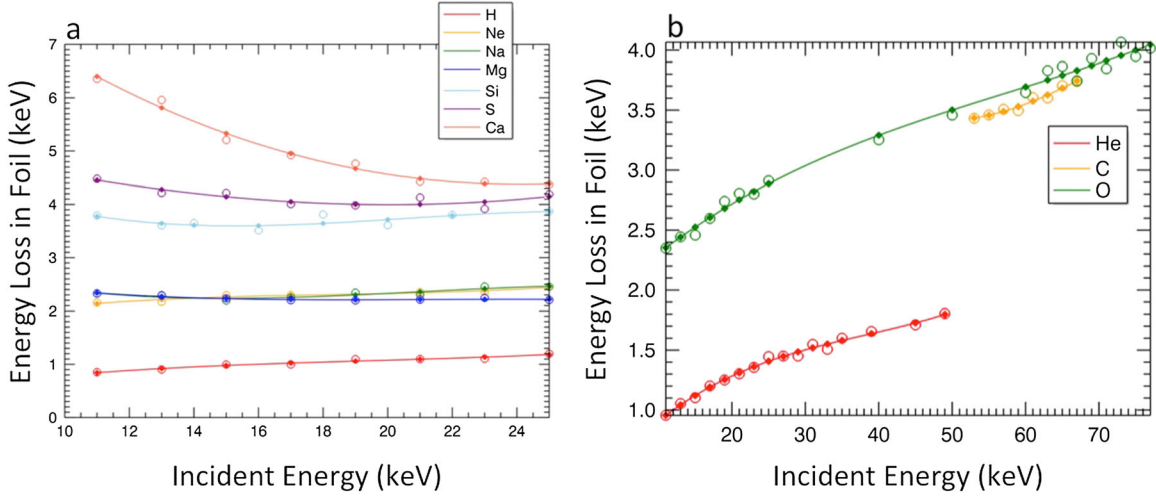


Figure A1. Energy loss in foil as a function of total ion energy from TRIM simulations. (a) Loss over an energy range appropriate for singly charged ions. (b) Loss over a larger energy range reflecting additional energy gained in postacceleration by multiply charged ions, up to O^{6+} .

accomplished with a simple TOF forward model that is calibrated with flight data. The TOF forward model is comprised of the following:

$$E_{\text{tot}} = q \left[\left(\frac{E}{q} \right)_{\text{ESA}} - V_{\text{PAV}} \right] - E_{\text{loss}} \quad (\text{A1})$$

$$v = 439 \sqrt{\left(\frac{E_{\text{tot}}}{m} \right)} \quad (\text{A2})$$

$$\text{TOF} = 10^4 \frac{d}{v} - \tau_e - \tau_{\text{MCP}} \quad (\text{A3})$$

[64] Equation (A1) relates the total energy (E_{tot} , in keV) to the E/q (in keV/e) measured by the electrostatic analyzer (ESA), the additional energy supplied by postacceleration (V_{PAV} , a negative voltage, in kV), and the energy lost from passage through the carbon foil (E_{loss} , in keV). With E_{tot} in hand, the velocity (v , in km/s) of the ion in the TOF chamber can be calculated via equation (A2). Finally, the expected TOF (in ns) is calculated via equation (A3) from the known flight distance (d , in cm) and with corrections for the flight time of electrons from the carbon foil to the start microchannel plate (MCP) (τ_e , in ns) and detection times within the MCP (τ_{MCP} , in ns).

[65] The energy lost from passage through the carbon foil (E_{loss}) depends on the incident energy and mass of a particular ion, but not on the charge. This quantity was measured in laboratory calibrations for FIPS, but not for all possible ion species and energies. In this work, E_{loss} was derived from the modeled carbon foil interactions using the Transport of Ions in Matter (TRIM) software [Ziegler, 2004; Ziegler *et al.*, 2010]. For each element and total energy to be used in the analysis, 10^5 atoms were run through TRIM, producing a statistical distribution of energy loss values for that particular element and total energy combination. The peak energies for all of these runs were determined and used to make a polynomial fit of energy loss versus total energy for each element, shown in Figure A1.

[66] The forward model was implemented in a computer code that produced tracks in E/q -TOF space for each ion analyzed. These tracks were overlaid onto long accumulations of orbital data, from which specific ion tracks are clearly evident (Figure A2). This procedure allowed for calibration of the model by comparison of the alignment of model tracks and measured tracks. The ability to see clearly the alignment of the modeled tracks with observed data from long accumulations allowed the use of the same model under much lower signal-to-noise ratios typically present when analyzing individual FIPS scans.

[67] There are several limitations of this technique. Without being able to distinguish individual ion tracks, it is impossible

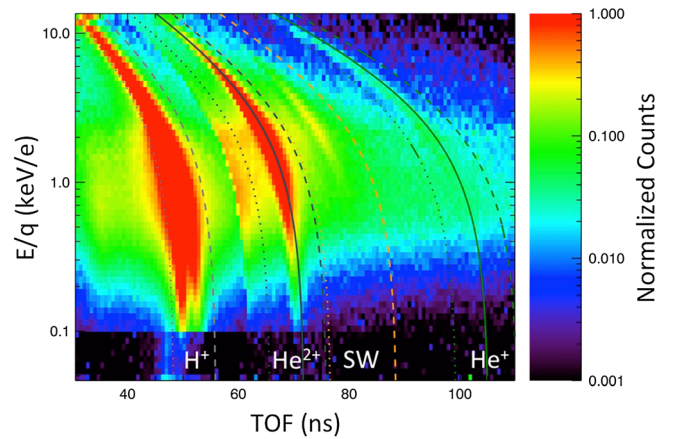


Figure A2. Accumulated raw FIPS event data from 25 March 2011 through 22 November 2011 together with lines showing the lower (dotted) and upper (dashed) bounds on modeled TOF as a function of E/q for each species. The modeled TOF center as a function of E/q (solid) is also shown in green for He^{2+} and He^+ . Counts are normalized to the maximum value. Background removal has not yet been completed for the data shown in this figure. The darker region below 0.1 keV/e is due to less time spent observing in this energy range.

to specify uniquely the set of ions identified in the analysis. Ions were selected that best fit the observations among those expected from studies of the neutral exosphere. Furthermore, where ion tracks overlap, due to TOF uncertainties (track width), no attempt was made to distribute statistically the counts to individual species. Rather, a composite track was constructed that includes the full range of TOF values for the corresponding group of ions. The consequences of this procedure are expected to be minor. Among the set of ions and groups chosen, no overlap was present.

[68] Some estimation of the error in the reported abundances can be made. Systematic errors, partly due to TOF overlap described above, are estimated at ~20%. Additional errors come from uncertainties due to counting (Poisson) statistics. Thus, the total error (ε) is calculated from

$$\varepsilon = \sqrt{(0.20)^2 + \left(\sqrt{N}/N\right)^2} \quad (\text{A4})$$

where N is the number of counts.

[69] **Acknowledgments.** This work was supported by NASA's Graduate Student Research Program and the MESSENGER mission. The MESSENGER project is supported by the NASA Discovery Program under contracts NAS5-97271 to The Johns Hopkins University Applied Physics Laboratory and NASW-00002 to the Carnegie Institution of Washington. NASA's Astrophysics Data System has been used extensively for this work. J.M.R. thanks Jonathan W. Thomas for designing and programming FIPS software libraries and Mark O. Stakhiv for suggesting one of the key visualizations used in this work.

References

- Anderson, B. J., C. L. Johnson, H. Korth, M. E. Purucker, R. M. Winslow, J. A. Slavin, S. C. Solomon, R. L. McNutt Jr., J. M. Raines, and T. H. Zurbuchen (2011), The global magnetic field of Mercury from MESSENGER orbital observations, *Science*, **333**, 1859–1862, doi:10.1126/science.1211001.
- Anderson, B. J., C. L. Johnson, H. Korth, R. M. Winslow, J. E. Borovsky, M. E. Purucker, J. A. Slavin, S. C. Solomon, M. T. Zuber, and R. L. McNutt Jr. (2012), Low-degree structure in Mercury's planetary magnetic field, *J. Geophys. Res.*, **117**, E00L12, doi:10.1029/2012JE004159.
- Andrews, G. B., et al. (2007), The Energetic Particle and Plasma Spectrometer instrument on the MESSENGER spacecraft, *Space Sci. Rev.*, **131**, 523–556, doi:10.1007/s11214-007-9272.
- Baker, D. N., et al. (2013), Solar wind forcing at Mercury: WSA-ENLIL model results, *J. Geophys. Res. Space Physics*, **118**, 45–57, doi:10.1029/2012JA018064.
- Baumgardner, J., and M. Mendillo (2009), The use of small telescopes for spectral imaging of low-light-level extended atmospheres in the Solar System, *Earth Moon Planets*, **105**, 107–113, doi:10.1007/s11038-009-9314-y.
- Baumgardner, J., J. Wilson, and M. Mendillo (2008), Imaging the sources and full extent of the sodium tail of the planet Mercury, *Geophys. Res. Lett.*, **35**, L03201, doi:10.1029/2007GL032337.
- Bida, T. A., R. M. Killen, and T. H. Morgan (2000), Discovery of calcium in Mercury's atmosphere, *Nature*, **404**, 159–161.
- Benna, M., et al. (2010), Modeling of the magnetosphere of Mercury at the time of the first MESSENGER flyby, *Icarus*, **209**, 3–10, doi:10.1016/j.icarus.2009.11.036.
- Broadfoot, A. L., S. Kumar, M. J. S. Belton, and M. B. McElroy (1974), Mercury's atmosphere from Mariner 10: Preliminary results, *Science*, **185**, 166–169, doi:10.1126/science.185.4146.166.
- Cheng, A. F., R. E. Johnson, S. M. Krimigis, and L. J. Lanzerotti (1987), Magnetosphere, exosphere and surface of Mercury, *Icarus*, **71**, 430–440.
- Delcourt, D. C., T. E. Moore, S. Orsini, A. Milillo, and J.-A. Sauvaud (2002), Centrifugal acceleration of ions near Mercury, *Geophys. Res. Lett.*, **29**, L01591, doi:10.1029/2001GL013829.
- Delcourt, D. C., S. Grimald, F. Leblanc, J.-J. Berthelier, A. Milillo, A. Mura, S. Orsini, and T. E. Moore (2003), A quantitative model of the planetary Na⁺ contribution to Mercury's magnetosphere, *Annal. Geophys.*, **21**, 1723–1736, doi:10.5194/angeo-21-1723-2003.
- Domingue, D. L., P. L. Koehn, R. M. Killen, A. L. Sprague, M. Sarantos, A. F. Cheng, E. T. Bradley, and W. E. McClintock (2007), Mercury's atmosphere: A surface-bounded exosphere, *Space Sci. Rev.*, **131**, 161–186, doi:10.1007/s11214-007-9260-9.
- Dungey, J. W. (1961), Interplanetary magnetic field and the auroral zones, *Phys. Rev. Lett.*, **6**, 47–48, doi:10.1103/PhysRevLett.6.47.
- Gershman, D. J., T. H. Zurbuchen, L. A. Fisk, J. A. Gilbert, J. M. Raines, B. J. Anderson, C. W. Smith, H. Korth, and S. C. Solomon (2012), Solar wind alpha particles and heavy ions in the inner heliosphere, *J. Geophys. Res.*, **117**, A00M02, doi:10.1029/2012JA017829.
- Hartle, R. E., and G. E. Thomas (1974), Neutral and ion exosphere models for lunar hydrogen and helium, *J. Geophys. Res.*, **79**, 1519–1526, doi:10.1029/JA079i010p01519.
- Hartle, R. E., S. A. Curtis, and G. E. Thomas (1975), Mercury's helium exosphere, *J. Geophys. Res.*, **80**, 3689–3692, doi:10.1029/JA080i025p03689.
- Hartle, R. E., M. Sarantos, and E. C. Sittler Jr. (2011), Pickup ion distributions from three-dimensional neutral exospheres, *J. Geophys. Res.*, **116**, A10101, doi:10.1029/2011JA016859.
- Hesterberg T. C., D. S. Moore, S. Monaghan, A. Clipson, R. Epstein, B. A. Craig, and G. P. McCabe (2010), Bootstrap methods and permutation tests, in *Introduction to the Practice of Statistics*, 7th ed., edited by D. S. Moore, G. P. McCabe and B. A. Craig, W. H. Freeman, New York.
- Hesterberg, T. (2011), Bootstrap, *Wiley Interdisciplinary Reviews: Computational Statistics*, **3**, 497–526, doi:10.1002/wics.182.
- Killen, R. M. (2003), Depletion of sulfur on the surface of asteroids and the Moon, *Meteorit. Planet. Sci.*, **38**, 383–388, doi:10.1111/j.1945-5100.2003.tb00273.x.
- Killen, R. M., A. E. Potter, and T. H. Morgan (1990), Spatial distribution of sodium vapor in the atmosphere of Mercury, *Icarus*, **85**, 145–167, doi:10.1016/0019-1035(90)90108-L.
- Killen, R. M., A. Potter, A. Fitzsimmons, and T. H. Morgan (1999), Sodium D2 line profiles: Clues to the temperature structure of Mercury's exosphere, *Planet. Space Sci.*, **47**, 1449–1458, doi:10.1016/S0032-0633(99)00071-9.
- Killen, R. M., A. E. Potter, P. Reiff, M. Sarantos, B. V. Jackson, P. Hick, and B. Giles (2001), Evidence for space weather at Mercury, *J. Geophys. Res.*, **106**, 20,509–20,526, doi:10.1029/2000JE001401.
- Killen, R. M., M. Sarantos, and P. H. Reiff (2004), Space weather at Mercury, *Adv. Space Res.*, **33**, 1899–1904, doi:10.1016/j.asr.2003.02.020.
- Killen, R. M., T. A. Bida, and T. H. Morgan (2005), The calcium exosphere of Mercury, *Icarus*, **173**, 300–311, doi:10.1016/j.icarus.2004.08.022.
- Killen, R., G. Cremonese, H. Lammer, S. Orsini, A. E. Potter, A. L. Sprague, P. Wurz, M. L. Khodachenko, H. I. M. Lichtenegger, A. Milillo, and A. Mura (2007), Processes that promote and deplete the exosphere of Mercury, *Space Sci. Rev.*, **132**, 433–509, doi:10.1007/s11214-007-9232-0.
- Leblanc, F., and J. Y. Chaufray (2011), Mercury and Moon He exospheres: Analysis and modeling, *Icarus*, **216**, 551–559, doi:10.1016/j.icarus.2011.09.028.
- Leblanc, F., and R. E. Johnson (2003), Mercury's sodium exosphere, *Icarus*, **164**, 261–281.
- Leblanc, F., and R. E. Johnson (2010), Mercury exosphere I. Global circulation model of its sodium component, *Icarus*, **209**, 280–300, doi:10.1016/j.icarus.2010.04.020.
- Leblanc, F., D. Delcourt, and R. E. Johnson (2003), Mercury's sodium exosphere: Magnetospheric ion recycling, *J. Geophys. Res.*, **108**, 5136–5147, doi:10.1029/2003JE002151.
- Lukyanov, A. V., O. Umnova, and S. Barabash (2001), Energetic neutral atom imaging of Mercury's magnetosphere, 1. Distribution of neutral particles in an axially symmetrical exosphere, *Planet. Space Sci.*, **49**, 1669–1675, doi:10.1016/S0032-0633(01)00105-2.
- Massetti, S., S. Orsini, A. Milillo, A. Mura, E. de Angelis, H. Lammer, and P. Wurz (2003), Mapping of the cusp plasma precipitation on the surface of Mercury, *Icarus*, **166**, 229–237, doi:10.1016/j.icarus.2003.08.005.
- McClintock, W. E., R. J. Vervack Jr., E. T. Bradley, R. M. Killen, N. Mouawad, A. L. Sprague, M. H. Burger, S. C. Solomon, and N. R. Izenberg (2009), MESSENGER observations of Mercury's exosphere: Detection of magnesium and distribution of constituents, *Science*, **324**, 610–613.
- Misawa, H., A. Sonobe, A. Morioka, and S. Okano (2008), Investigation of local time dependence of Mercury's sodium exosphere based on a numerical simulation, *Planet. Space Sci.*, **56**, 1681–1687, doi:10.1016/j.pss.2008.07.029.
- Mura, A., A. Milillo, S. Orsini, and S. Massetti (2007), Numerical and analytical model of Mercury's exosphere: Dependence on surface and external conditions, *Planet. Space Sci.*, **55**, 1569–1583, doi:10.1016/j.pss.2006.11.028.
- Ogilvie, K. W., J. D. Scudder, R. E. Hartle, G. L. Siscoe, H. S. Bridge, A. J. Lazarus, J. R. Asbridge, S. J. Bame, and C. M. Yeates (1974), Observations at Mercury encounter by the plasma science experiment on Mariner 10, *Science*, **185**, 145–151, doi:10.1126/science.185.4146.145.
- Potter, A. E., and T. H. Morgan (1990), Evidence for magnetospheric effects on the sodium atmosphere of Mercury, *Science*, **248**, 835–838, doi:10.1126/science.248.4957.835.
- Potter, A. E., and T. H. Morgan (1997), Evidence for suprathermal sodium on Mercury, *Adv. Space Res.*, **19**, 1571–1576, doi:10.1016/S0273-1177(97)00370-0.

- Potter, A. E., R. M. Killen, and T. H. Morgan (1999), Rapid changes in the sodium exosphere of Mercury, *Planet. Space Sci.*, 47, 1441–1448, doi:10.1016/S0032-0633(99)00070-7.
- Potter, A. E., R. M. Killen, and T. H. Morgan (2002), The sodium tail of Mercury, *Meteorit. Planet. Sci.*, 37, 1165–1172, doi:10.1111/j.1945-5100.2002.tb00886.x.
- Potter, A. E., R. M. Killen, and T. H. Morgan (2007), Solar radiation acceleration effects on Mercury sodium emission, *Icarus*, 186, 571–580, doi:10.1016/j.icarus.2006.09.025.
- Raines, J. M., J. A. Slavin, T. H. Zurbuchen, G. Gloeckler, B. J. Anderson, D. N. Baker, H. Korth, S. M. Krimigis, and R. L. McNutt Jr. (2011), MESSENGER observations of the plasma environment near Mercury, *Planet. Space Sci.*, 59, 2004–2015, doi:10.1016/j.pss.2011.02.004.
- Russell, C. H., D. N. Baker, J. A. Slavin (1988), The magnetosphere of Mercury, in *Mercury*, edited by F. Vilas, C. R. Chapman, and M. S. Matthews, pp. 514–561, Univ. of Arizona Press, Tucson, Ariz.
- Sarantos, M., P. H. Reiff, T. W. Hill, R. M. Killen, and A. L. Urquhart (2001), A B_z -interconnected magnetosphere model for Mercury, *Planet. Space Sci.*, 49, 1629–1635, doi:10.1016/S0032-0633(01)00100-3.
- Sarantos, M., R. M. Killen, and D. Kim (2007), Predicting the long-term solar wind ion-sputtering source at Mercury, *Planet. Space Sci.*, 55, 1584–1595, doi:10.1016/j.pss.2006.10.011.
- Sarantos, M., R. M. Killen, W. E. McClintock, E. T. Bradley, R. J. Vervack Jr., M. Benna, and J. A. Slavin (2011), Limits to Mercury’s magnesium exosphere from MESSENGER second flyby observations, *Planet. Space Sci.*, 59, 1992–2003, doi:10.1016/j.pss.2011.05.002.
- Schmidt, C. A., J. Baumgardner, M. Mendillo, and J. K. Wilson (2012), Escape rates and variability constraints for high-energy sodium sources at Mercury, *J. Geophys. Res.*, 117, A03301, doi:10.1029/2011JA017217.
- Slavin, J. A. (2004), Mercury’s magnetosphere, *Adv. Space Res.*, 33, 1859–1874, doi:10.1016/j.asr.2003.02.019.
- Slavin, J. A., and R. E. Holzer (1979), The effect of erosion on the solar wind stand-off distance at Mercury, *J. Geophys. Res.*, 84, 2076–2082, doi:10.1029/JA084iA05p02076.
- Slavin, J. A., et al. (2009), MESSENGER observations of magnetic reconnection in Mercury’s magnetosphere, *Science*, 324, 606–610, doi:10.1126/science.1172011.
- Solomon, S. C., R. L. McNutt Jr., R. E. Gold, and D. L. Domingue (2007), MESSENGER mission overview, *Space Sci. Rev.*, 131, 3–39, doi:10.1007/s11214-007-9247-6.
- Spreiter, J. R., A. L. Summers, and A. Y. Alksne (1966), Hydromagnetic flow around the magnetosphere, *Planet. Space Sci.*, 14, 223–253, doi:10.1016/0032-0633(66)90124-3.
- Sprague, A. L., R. W. H. Kozlowski, D. M. Hunten, N. M. Schneider, D. L. Domingue, W. K. Wells, W. Schmitt, and U. Fink (1997), Distribution and abundance of sodium in Mercury’s atmosphere, 1985–1988, *Icarus*, 129, 506–527, doi:10.1006/icar.1997.5784.
- Sprague, A. L., W. J. Schmitt, and R. E. Hill (1998), Mercury: Sodium atmospheric enhancements, radar-bright spots, and visible surface features, *Icarus*, 136, 60–68, doi:10.1006/icar.1998.6009.
- Wang, Y.-C. and W. -H. Ip (2011), Source dependency of exospheric sodium on Mercury, *Icarus*, 216, 387–402.
- Winslow, R. M., B. J. Anderson, C. L. Johnson, J. A. Slavin, H. Korth, M. E. Purucker, D. N. Baker, and S. C. Solomon (2013), Mercury’s magnetopause and bow shock from MESSENGER Magnetometer observations, *J. Geophys. Res. Space Physics*, doi:10.1002/jgra.50237, in press.
- Yagi, M., K. Seki, Y. Matsumoto, D. C. Delcourt, and F. Leblanc (2010), Formation of a sodium ring in Mercury’s magnetosphere, *J. Geophys. Res.*, 115, A10253, doi:10.1029/2009JA015226.
- Ziegler, J. F. (2004), SRIM-2003, *Nucl. Instrum. Methods Phys. Res. B*, 219, 1027–1036, doi:10.1016/j.nimb.2004.01.208.
- Ziegler, J. F., Ziegler, M. D., and J. P. Biersack (2010), SRIM - The stopping and range of ions in matter (2010), *Nucl. Instrum. Methods Phys. Res. B*, 268, 1818–1823, doi:10.1016/j.nimb.2010.02.091.
- Zurbuchen, T. H., G. Gloeckler, J. C. Cain, S. E. Lasley, and W. Shanks (1998), A low-weight plasma instrument to be used in the inner heliosphere, in *Conference on Missions to the Sun II*, edited by C. M. Korendyke, Proceedings of the Society of Photo-Optical Instrumentation Engineers, 3442, 217–224.
- Zurbuchen, T. H., P. Koehn, L. A. Fisk, T. Gombosi, G. Gloeckler, and K. Kabin (2004), On the space environment of Mercury, *Adv. Space Res.*, 33, 188–1889, doi:10.1016/j.asr.2003.04.048.
- Zurbuchen, T. H., J. M. Raines, G. Gloeckler, S. M. Krimigis, J. A. Slavin, P. L. Koehn, R. M. Killen, A. L. Sprague, R. L. McNutt Jr., and S. C. Solomon (2008), MESSENGER observations of the composition of Mercury’s ionized exosphere and plasma environment, *Science*, 321, 90–92, doi:10.1126/science.1159314.
- Zurbuchen, T. H., et al. (2011), MESSENGER observations of the spatial distribution of planetary ions near Mercury, *Science*, 333, 1862–1865, doi:10.1126/science.1211302.